

LIGO SURF Final Report: 3D Localization of Gravitational Wave Event Candidates

Patricia Porter*
Carleton College

Larry Price[†], Leo Singer[‡], Vivien Raymond[§]
LIGO SURF Advisors, California Institute of Technology

September 24, 2013

Advanced LIGO and Virgo sensitivities to gravitational waves enable the prospect of making joint electromagnetic observations of the mergers between binary systems containing two neutron stars or a neutron star and a black hole. Gravitational wave signals can be used to localize their source's sky position, enabling telescopes to detect the corresponding electromagnetic counterpart. In this project, we assess the accuracy of our information from gravitational-wave triggers about the distance to the source and look at ways of combining this information with the source's probable sky location for more effective electromagnetic follow-up campaigns.

1. Background

Gravitational wave (GW) observations provide new information about their sources, aiding in the development a more complete picture of astronomical phenomena. Analogous to the production of electromagnetic (EM) waves by accelerated charges, GWs are generated by accelerated mass distributions, such as supernova explosions or mergers of neutron star and black hole binary systems. Such events induce the propagation of GWs through our universe at the speed of light, resulting in the alternating stretching and compressing of space-time transverse to the direction of propagation [1]. Current GW detectors, such as those used by aLIGO and Virgo, are Michelson-type laser interferometers that measure the effects of GW tidal forces through distance changes between mirrors suspended in vacuum within the detector [3]. Although indirect evidence of GW emission has been observed through its effects on the orbital evolution of pulsars, a GW has not yet been directly detected [4]. With recent efforts to increase detector sensitivity, the aLIGO and Virgo ground-based detectors are predicted to observe a GW signal within the next decade [5].

Unlike electromagnetic (EM) waves, which are emitted by individual particles, GWs are emitted by bulk motions of their source, and therefore, carry a completely different set of information about their origin [4]. For example, GW observations measure the masses and spins of their source's components with great accuracy. In addition, GWs can be used to approximate their source's sky location and distance [6] [4]. However, there are some properties, such as a source's redshift, that GWs cannot measure, but that can be determined from EM observation [5]. Considering the complementary information provided by GW and EM observation, the joint observation of both emissions would provide further insight into the nature of their source, such as its Hubble constant.

*porterp@carleton.edu

†lprice@caltech.edu

‡lsinger@caltech.edu

§vivien@caltech.edu

One of the most promising sources of coincident GW and EM emissions in the frequency range of current detectors is the merger between two neutron stars or a neutron star and a black hole, known as a compact binary coalescence (CBC) event [5]. During the inspiral of a CBC event, the neutron star may be torn apart, resulting in EM emission across the spectrum that can last anywhere from seconds to months after the event [3]. Finding the EM counterpart of a GW would not only help to validate a GW detection, but would also provide a more accurate measurement of the luminosity distance to the source and refine the source's sky localization [7].

In order to obtain optimal EM follow-up of GW candidates, GW signals can be used to localize their source's sky position, enabling the ideal orientation of telescopes to detect the corresponding EM counterpart [9]. GW detectors are designed to receive signals from a large fraction of the sky, and, consequentially, a single detector provides little information about the sky location of a detection's source. However, using a network of detectors, one can triangulate a CBC event from the observed time delays in the GW signals at several detector sites. Using timing information alone, it is only possible to determine the sky location of a detection's source as projected onto the baseline of the detectors. Therefore, localization can only restrict a source's sky position up to the reflection degeneracy with respect to the plane of the detectors. For networks consisting of more than two detectors, such as the aLIGO-Virgo detector network, this mirror image degeneracy can usually be mitigated by requiring consistency between the observed amplitudes of signals from each detector [7].

The observed time delays and amplitude of a GW signal can then be used to determine a probability distribution of a source's most likely sky location. In general, the posterior distribution for the set of parameters $\boldsymbol{\mu}$, given the dataset s , can be found using Bayes' theorem [7],

$$p(\boldsymbol{\mu}|s) = \frac{p(\boldsymbol{\mu})p(s|\boldsymbol{\mu})}{p(s)} = \frac{p(\boldsymbol{\mu})p(s|\boldsymbol{\mu})}{\int d\boldsymbol{\mu} p(\boldsymbol{\mu})p(s|\boldsymbol{\mu})}. \quad (1)$$

In this equation, $p(\boldsymbol{\mu})$ is the prior probability distribution of the parameters $\boldsymbol{\mu}$, $p(s|\boldsymbol{\mu})$ is the likelihood that the dataset s is consistent with the parameters $\boldsymbol{\mu}$, and $p(s)$ is the marginal likelihood given by the distribution of the observed data s marginalized over the parameters $\boldsymbol{\mu}$ [8]. The set of parameters $\boldsymbol{\mu}$ defining a GW signal includes the following parameters,

$$\boldsymbol{\mu} = (\theta, \phi, r, t_c, \phi_c, \iota, m_1, m_2), \quad (2)$$

where θ is the right ascension, ϕ is the declination, r is the distance to the source, t_c is the coalescence time, ϕ_c is the orbital phase at coalescence, ι is the inclination angle of the orbital, and m_1 and m_2 are the masses of the binary components [3]. However, in order to determine the probability distribution of a source's sky location, it is only necessary to consider a subset of these parameters, particularly the right ascension and declination. This is made possible by either fixing or marginalizing over all other parameters except for those related to the sky position of the source [7]. The likelihood $p(s|\boldsymbol{\mu})$ can be determined by the likelihood ratio of a signal h parametrized by $\boldsymbol{\mu}$ being present in the dataset s , relative to the null hypothesis. This is given by [7]

$$\Lambda(\boldsymbol{\mu}) = \frac{p(s|h(\boldsymbol{\mu}))}{p(s|0)} = \frac{e^{-\langle s-h(\boldsymbol{\mu})|s-h(\boldsymbol{\mu}) \rangle/2}}{e^{-\langle s|s \rangle/2}}, \quad (3)$$

where the inner product is defined in terms of the noise power spectrum of the detector $S(f)$ by the integral [7]

$$\langle a|b \rangle = 4Re \int_0^\infty df \frac{\bar{a}(f)\bar{b}^*(f)}{S(f)}. \quad (4)$$

Using this calculation of the likelihood $p(s|\mu)$ and assuming a uniform prior distribution $p(\mu)$, one can obtain a probability distribution of a source's sky location from the amplitude and observed time delays of its GW signal. This probability distribution, referred to as a GW skymap, can then be used to guide telescopes, optimizing the probability of EM detection. An example of a skymap is shown in Fig. 1 [7].

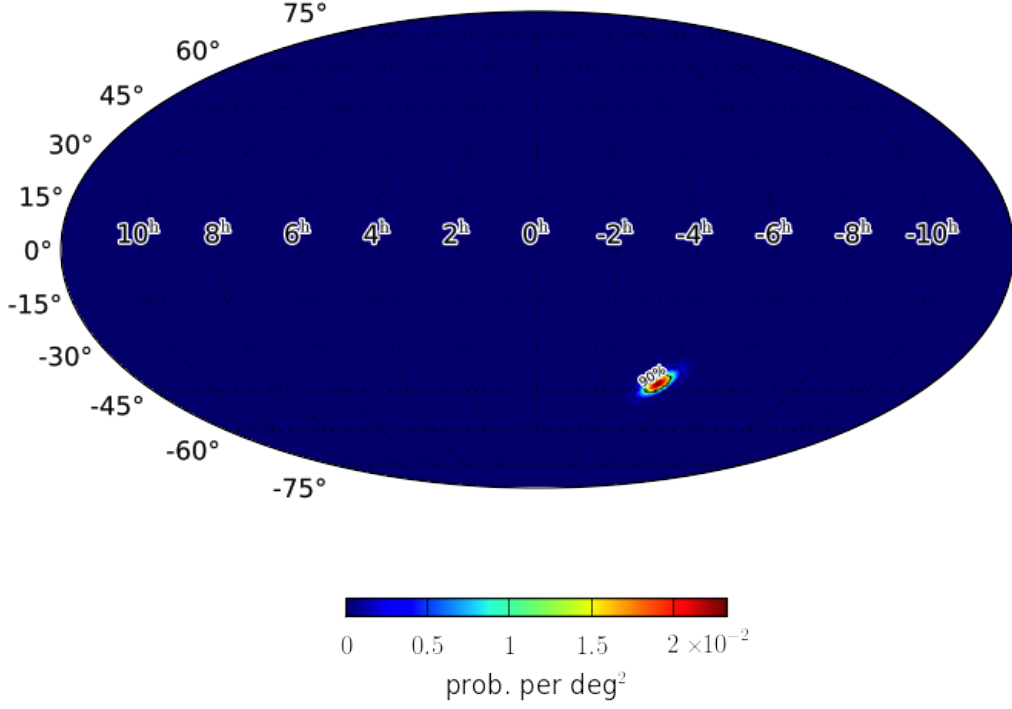


Figure 1: GW skymap for the G71031 trigger on February 16, 2013. More probable source locations are indicated in red, while less probable regions are in blue. Image from [10].

The primary source of error in using a network of detectors to create a GW skymap is due to the uncertainty in the timing accuracy of the GW signal. This is approximated to be

$$\sigma_t \approx \frac{1}{2\pi\sigma_f\rho}, \quad (5)$$

where ρ is the signal-to-noise ratio (SNR) and σ_f is the effective bandwidth of the signal [7]. Taking into consideration this uncertainty, for an ideal source with optimal orientation the LIGO-Virgo detector network can restrict the source's sky location to an area of approximately 20 square degrees. Typical localization is approximately twice this area [7] [11]. This GW error region is likely to contain over a hundred galaxies out to 100 Mpc, making the imaging of all possible galaxies in this region impractical [11]. However, by incorporating distance as a parameter within Bayes' theorem, it may be possible to determine a more precise posterior probability distribution.

2. Modivation

Previous studies have demonstrated how the incorporation of a source's distance can be used to enhance source localization. For example, Nuttall and Sutton [11] developed a ranking statistic for comparing galaxies within the GW error box of a signal's 2D skymap to determine the most probable host galaxy within this region. Their statistic compares the luminosities and distances of potential galaxies, favoring nearby, larger galaxies as more probable sources of detection. This statistic is given by [11]

$$R = e^{-\frac{\chi^2}{2}} \frac{L}{d^\alpha}, \quad (6)$$

where L is the blue-light luminosity of the potential host galaxy, d is the distance to the galaxy, α is a constant, and χ^2 is the chi-squared match between the measured and predicted arrival time of the GW signal at each detector. Using this ranking statistic, it is possible to correctly identify the true host galaxy of a CBC event approximately 20-50% of the time when imaging a single galaxy, depending on the masses of the binary members. This accuracy can be increased up to 30-60% by collectively imaging groups of galaxies using a larger field-of-view [11]. These probability estimates further improve as the number of images taken increases, as depicted in Fig. 2.

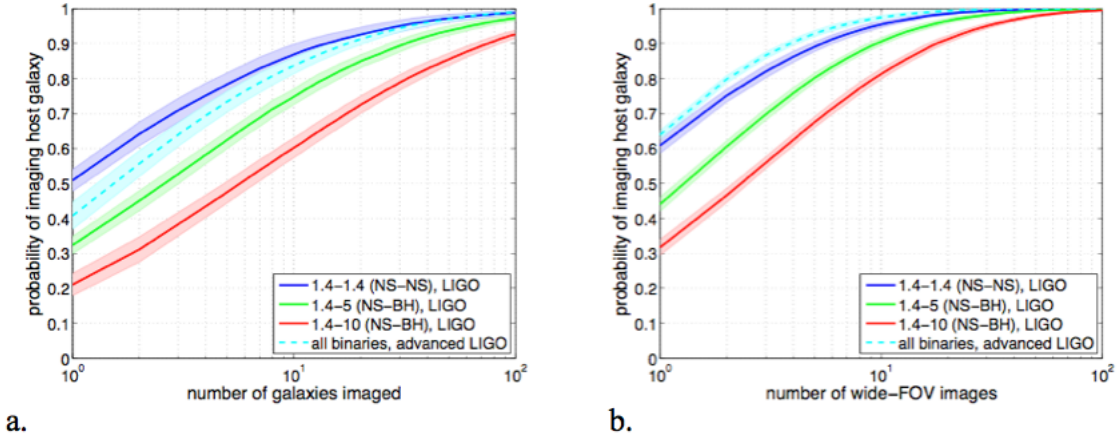


Figure 2: Probability of imaging a true host galaxy for various types of binary systems versus the number of images taken. The first graph (a) reflects the success rate of Nuttall and Sutton's statistic identifying the true host galaxy of a source when images are taken using a narrow field of view, whereas, the second graph (b) corresponds to a wide field of view. The shaded regions indicate the uncertainty associated with this probability estimate. Image from [11].

In this project, we examine the incorporation of the source's distance along with its sky location as parameters in Bayes' theorem to determine a 3D skymap of the most probable source locations. In this manner, we aim to take into consideration the actual distance to the source rather than just favoring closer galaxies. As described by Schutz [4], GW signals not only carry information about their source's sky position, but also about their distance. Using gravitational wave detectors, it is therefore possible to measure the effective distance to a source given by [7]

$$D_{eff} = D \left[F_+^2 \left(\frac{1 + \cos^2 \iota}{2} \right)^2 + F_x^2 \cos^2 \iota \right]^{-1/2}, \quad (7)$$

where D is the actual distance to the source, ι describes the inclination of the binary's orbital plane to our line-of-sight, and F_+ and F_\times are the antenna response functions of the detector.

In this paper, we assess the accuracy of our information from gravitational-wave triggers about the distance to their source and examine the incorporation this information with the source's probable sky location as parameters in Bayes' theorem to determine a 3D skymap of the most probable source locations. We then compare the efficiency and accuracy of the source localization performance of the resultant posterior probability distribution to that obtained using a 2D skymap.

3. Error Estimation

In order to analyze the accuracy of the parameter estimation obtained using Bayes' theorem, given in Eq. 1, we calculated the lower bound on the variance from the parameter estimations, known as the Cramér-Rao bound. This lower bound can be determined by the inverse of the Fisher information matrix. The elements of the Fisher matrix are given by

$$\mathcal{I}_{jk} = E \left[\frac{-\partial^2 \log \mathcal{L}}{\partial \mu_j \partial \mu_k} \middle| \boldsymbol{\mu} \right], \quad (8)$$

where $E[y]$ represents the expectation value of y and \mathcal{L} is the probability of observation x given the parameters $\boldsymbol{\mu}$, which is known as the likelihood.

The Fisher information matrix provides a simple way of determining a lower limit on the extent to which we can restrict various parameters of a GW signal. The Fisher matrix is convenient because assuming that the uncertainty in the parameters follows a Gaussian distribution, the elements of the Fisher matrix depends only on the likelihood \mathcal{L} , which is given by

$$\log(\mathcal{L}) = -\frac{1}{2} \int_0^\infty \frac{|x(\omega) - h(\omega, \boldsymbol{\mu})|^2}{S(\omega)} d\omega, \quad (9)$$

where $S(\omega)$ is the noise power spectrum of the detector and $h(\omega, \boldsymbol{\mu})$ is the GW signal. By differentiating the logarithm of the likelihood given in Eq. 9 with respect to two parameters μ_j and μ_k , we can reduce our expression for the elements of the Fisher information matrix in Eq. 8, resulting in the following equation

$$\mathcal{I}_{jk} = - \int_0^\infty \frac{\text{Re} \left[\left(\frac{\partial h}{\partial \mu_j} \right)^* \left(\frac{\partial h}{\partial \mu_k} \right) \right]}{S(\omega)} d\omega. \quad (10)$$

Modeling the GW signal $h(\omega)$ as a Newtonian chirp, $h(\omega)$ is defined by the linear combination of the two polarization components $h_+(\omega)$ and $h_\times(\omega)$

$$h(\omega) = F_+ h_+(\omega) + F_\times h_\times(\omega), \quad (11)$$

where F_+ and F_\times are the detector's antenna-pattern. To simplify $h(\omega)$, we assume that the GW's source is in line perpendicular to the arms of the detector such that the inclination of the orbital to the line of sight is zero degrees. In this case, $h(\omega)$ reduces to

$$h(\omega) = A e^{i(\gamma - \omega\tau)} h_0(\omega), \quad (12)$$

where A , γ , and τ are related to the inverse distance to the source, the phase of the signal, and the time of coalescence respectively. In Eq. 12, $h_0(\omega)$ is given by

$$h_0(\omega) = \mathcal{M}^{5/6} \left(\frac{G\omega}{2c^3} \right)^{-7/6} e^{-i\Psi(\omega)}, \quad (13)$$

where \mathcal{M} is the chirp mass, which is defined as

$$\mathcal{M} = M_{tot}\eta^{3/5} = M_{tot} \left(\frac{m_1 m_2}{M_{tot}^2} \right)^{3/5}, \quad (14)$$

where m_1 and m_2 are the masses of the binary components of the inspiral and η is the reduced mass over the total mass of these components. In addition, the term $\Psi(\omega)$, also introduced in Eq. 13, can be approximated as

$$\Psi(\omega) \approx -\frac{\pi}{4} + \frac{3}{128} \left(\frac{G\mathcal{M}\omega}{2c^3} \right)^{-5/3}. \quad (15)$$

Combining this expression for $\Psi(\omega)$ with the expression for $h_0(\omega)$ in Eq. 13 and plugging this into the equation for the GW signal $h(\omega)$ given in Eq. 12, we derive an expression for $h(\omega)$ dependent on the parameters A , γ , τ , and \mathcal{M} . Using the expression for \mathcal{I}_{jk} given in Eq. 10, we then solved for the elements of the Fisher information matrix with respect to each of these parameters, as shown below.

$$\begin{matrix} & \rho & \gamma & \tau & \mathcal{M} \\ \rho & \left(\begin{array}{cccc} 1 & 0 & 0 & \frac{5\rho}{6\mathcal{M}} \\ 0 & \rho^2 & -\rho^2\bar{\omega} & \frac{5\rho^2}{128\mathcal{M}} \left(\frac{G\mathcal{M}}{2c^3} \right)^{-5/3} \omega^{-5/3} \\ 0 & -\rho^2\bar{\omega} & \rho^2\omega^2 & -\frac{5\rho^2}{128\mathcal{M}} \left(\frac{G\mathcal{M}}{2c^3} \right)^{-5/3} \omega^{-2/3} \\ \frac{5\rho}{6\mathcal{M}} & \frac{5\rho^2}{128\mathcal{M}} \left(\frac{G\mathcal{M}}{2c^3} \right)^{-5/3} \omega^{-5/3} & -\frac{5\rho^2}{128\mathcal{M}} \left(\frac{G\mathcal{M}}{2c^3} \right)^{-5/3} \omega^{-2/3} & \left(\frac{5\rho}{2\mathcal{M}} \right)^2 \left[\frac{1}{9} + \frac{1}{4096} \left(\frac{G\mathcal{M}}{2c^3} \right)^{-10/3} \omega^{-10/3} \right] \end{array} \right) \end{matrix} \quad (16)$$

As shown in Eq. 16, for simplification we introduced the unitless variable ρ to encompass the parameter A , where ρ is defined as

$$\rho = A\sigma \quad (17)$$

and σ^2 is given by the integral

$$\sigma^2 = \int_0^\infty \frac{|h_0(\omega)|^2}{S(\omega)} d\omega. \quad (18)$$

We approximated σ^2 using a Riemann sum given values for $S(\omega)$ at discrete frequencies ranging from 9-8,190 Hz [13]. For every possible pairing of the four parameters \mathcal{M} , ρ , γ , and τ , we created 2x2 matrices corresponding to the elements of the Fisher matrix related to the two parameters. By inverting this matrix, we determined the covariance matrix of the following parameter pairs: \mathcal{M} and ρ , \mathcal{M} and γ , \mathcal{M} and τ , and γ and τ . We excluded the pairings of ρ and γ and ρ and τ because the partial derivative of $h(\omega)$ with respect to ρ is real whereas the partial derivatives with respect to γ and τ are imaginary, resulting in zeros within their respective 2x2 matrices. For each of the four aforementioned parameter pairs with nonzero elements, we created error ellipses. The semi-major and minor axes of each ellipse were defined by the square root of the eigenvalues of each covariance matrix corresponding to a parameter pair. In addition, the tilt of the ellipse was determined by the angle between the eigen vectors of each covariance matrix.

For each parameter pair, we analyzed error ellipses for a 1.4-1.4, 1.4-10, and 10-10 M_\odot inspiral, which correspond to a NS-NS, NS-BH, and BH-BH merger respectively. In addition, for each of

these types of inspirals, we considered when $\rho=5, 10$, and 15 . The resulting eighteen error ellipses for the parameter pairs \mathcal{M} and ρ and γ and τ are shown in Figs. 3-5.

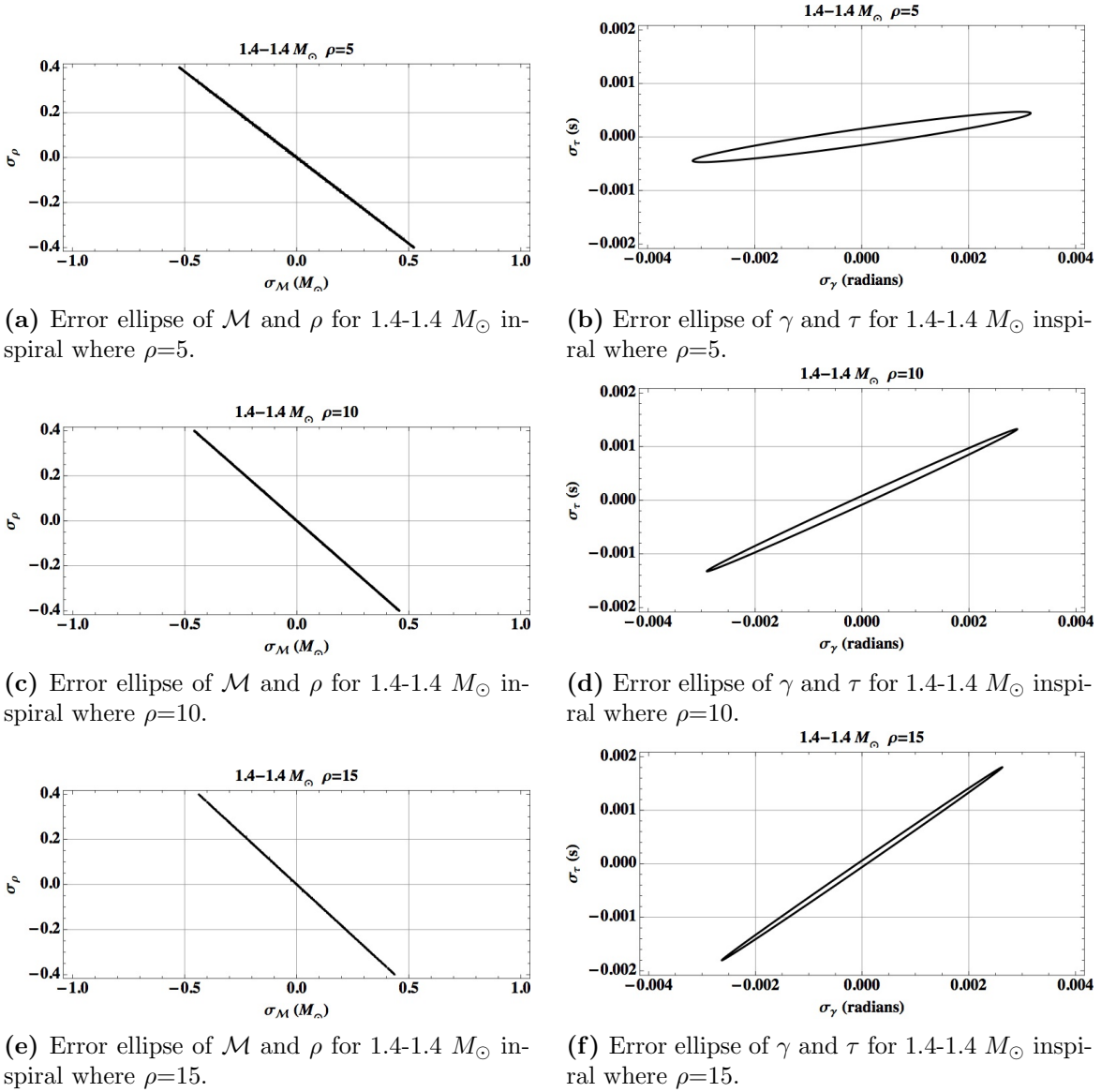
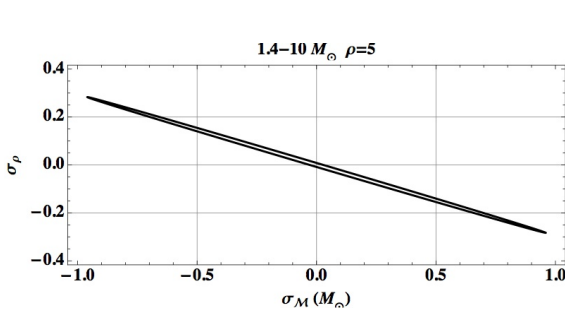
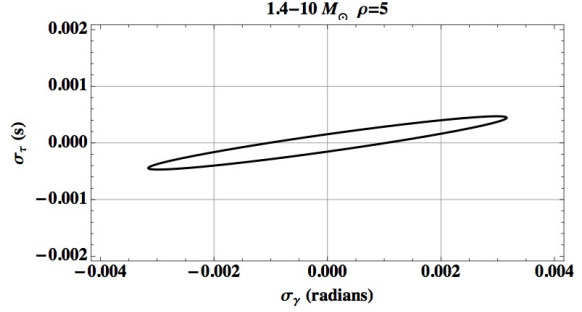


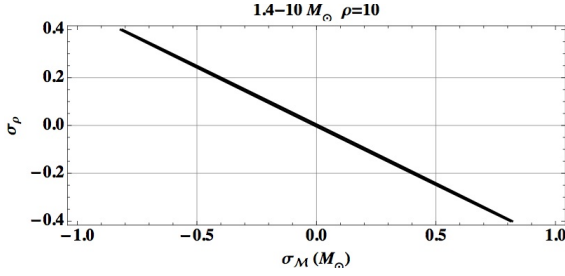
Figure 3: Error ellipses for a NS-NS M_\odot inspiral where $\rho=5, 10$, and 15 . Ellipses are shown for parameter pairs \mathcal{M} and ρ (left column) and γ and τ (right column). $\sigma_{\mathcal{M}}, \sigma_\rho, \sigma_\gamma$, and σ_τ represent the deviation from the estimated value of their respective parameter, which is centered at zero.



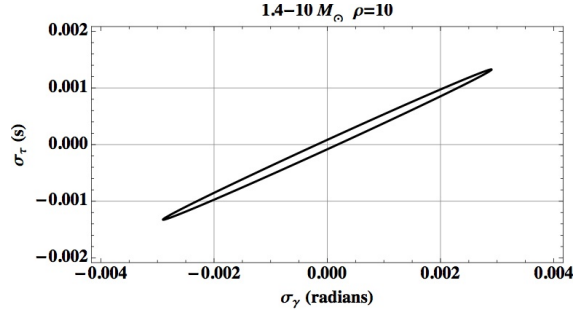
(a) Error ellipse of \mathcal{M} and ρ for $1.4-10 M_\odot$ inspiral where $\rho=5$.



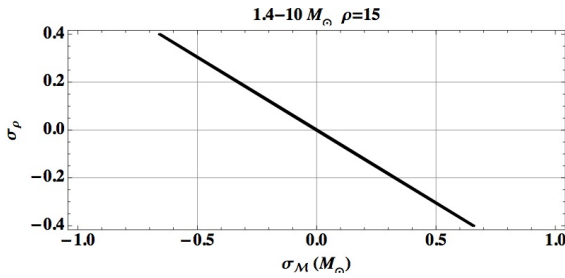
(b) Error ellipse of γ and τ for $1.4-10 M_\odot$ inspiral where $\rho=5$.



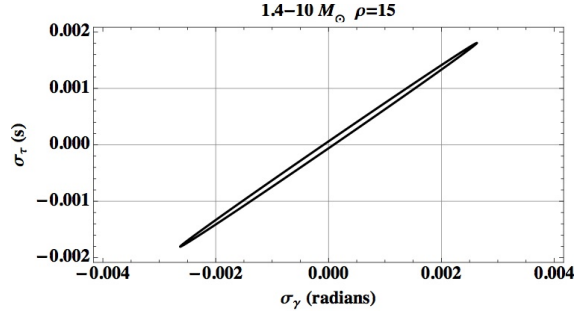
(c) Error ellipse of \mathcal{M} and ρ for $1.4-10 M_\odot$ inspiral where $\rho=10$.



(d) Error ellipse of γ and τ for $1.4-10 M_\odot$ inspiral where $\rho=10$.

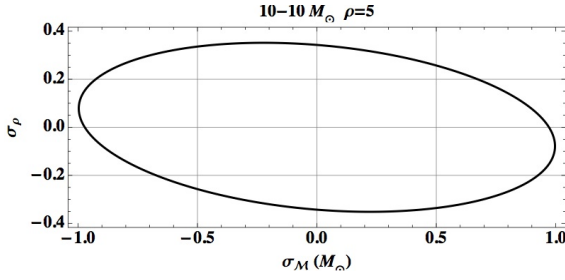


(e) Error ellipse of \mathcal{M} and ρ for $1.4-10 M_\odot$ inspiral where $\rho=15$.

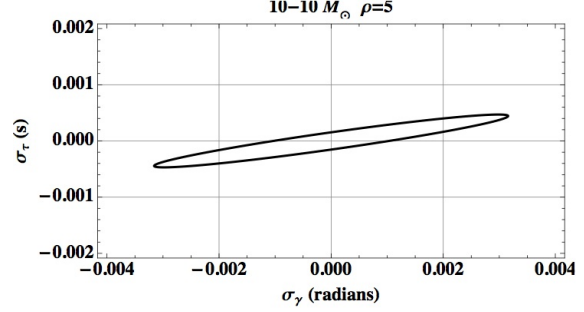


(f) Error ellipse of γ and τ for $1.4-10 M_\odot$ inspiral where $\rho=15$.

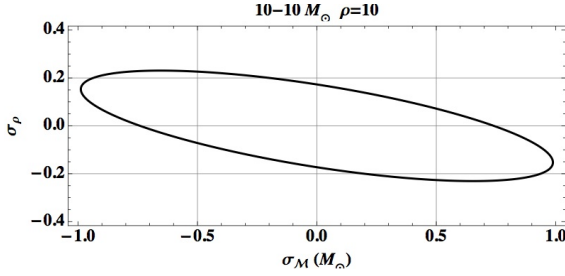
Figure 4: Error ellipses for a NS-BH M_\odot inspiral where $\rho=5, 10$, and 15 . Ellipses are shown for parameter pairs \mathcal{M} and ρ (left column) and γ and τ (right column). $\sigma_{\mathcal{M}}, \sigma_\rho, \sigma_\gamma$, and σ_τ represent the deviation from the estimated value of their respective parameter, which is centered at zero.



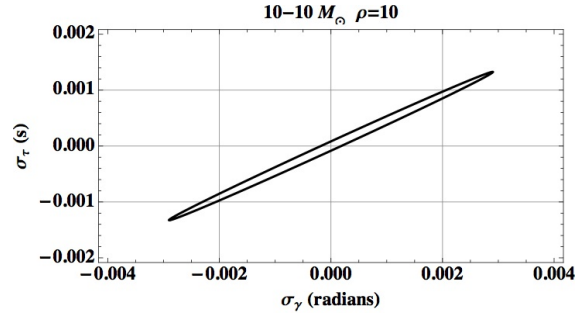
(a) Error ellipse of \mathcal{M} and ρ for 10-10 M_\odot inspiral where $\rho=5$.



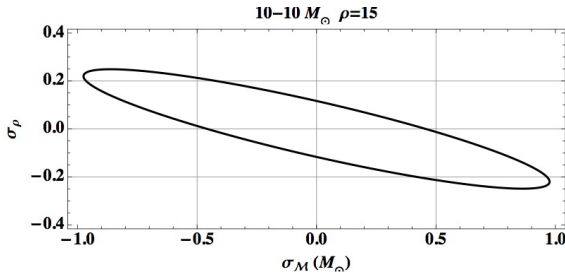
(b) Error ellipse of γ and τ for 10-10 M_\odot inspiral where $\rho=5$.



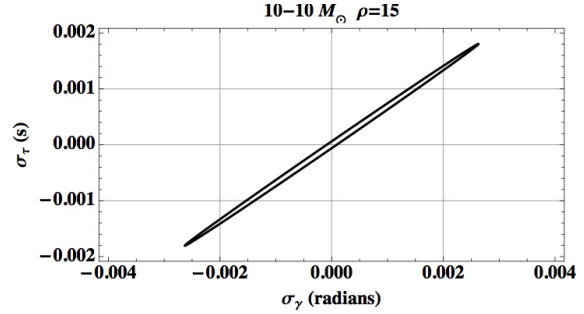
(c) Error ellipse of \mathcal{M} and ρ for 10-10 M_\odot inspiral where $\rho=10$.



(d) Error ellipse of γ and τ for 10-10 M_\odot inspiral where $\rho=10$.



(e) Error ellipse of \mathcal{M} and ρ for 10-10 M_\odot inspiral where $\rho=15$.



(f) Error ellipse of γ and τ for 10-10 M_\odot inspiral where $\rho=15$.

Figure 5: Error ellipses for a BH-BH M_\odot inspiral where $\rho=5$, 10, and 15. Ellipses are shown for parameter pairs \mathcal{M} and ρ (left column) and γ and τ (right column). $\sigma_{\mathcal{M}}$, σ_ρ , σ_γ , and σ_τ represent the deviation from the estimated value of their respective parameter, which is centered at zero.

From Figs. 3-5, we can see that the angle by which the ellipse is tilted increases as ρ increases and decreases as \mathcal{M} increases. In addition, as ρ increases the ellipses become more stretched out, indicating more accurate parameter estimations. Considering that ρ corresponds to one over the distance to the CBC event, the observed inverse relationship between the area of an ellipse and ρ suggests that the closer the source of a CBC event, the more accurately we can restrict its parameters. To better quantify the accuracy of the parameter estimation of ρ and its dependence on chirp mass, Fig. 6 shows σ_ρ as a function of \mathcal{M} .

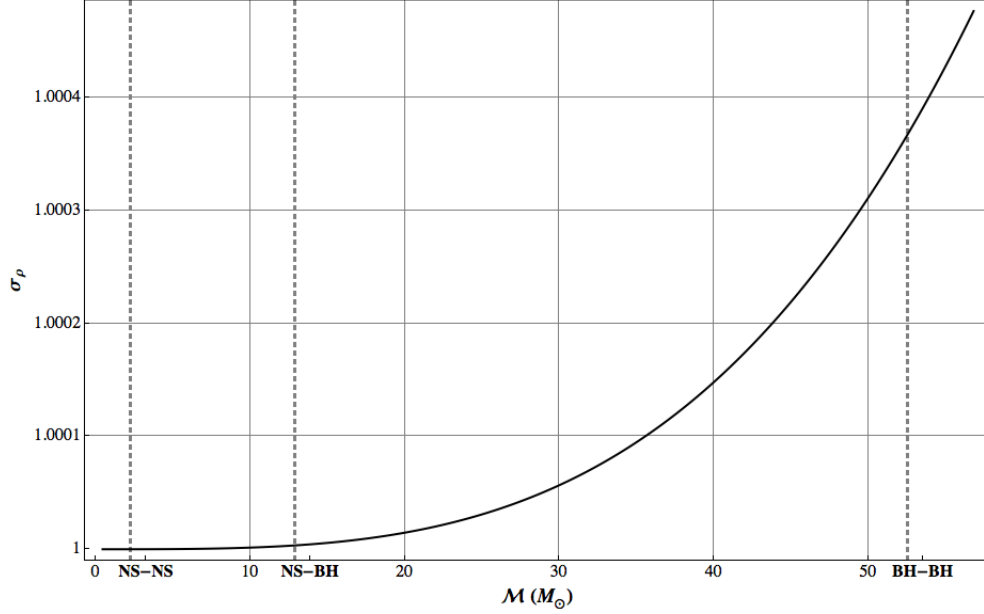


Figure 6: Uncertainty in ρ as a function of chirp mass. Chirp masses characteristic of a NS-NS, NS-BH, and BH-BH inspiral are denoted by dashed lines.

From Fig. 6, we can see that uncertainty in ρ increases exponentially as chirp mass increases. Hence, there is slightly more uncertainty in ρ for a NS-BH inspiral than a NS-NS inspiral. However, we can estimate the SNR for a NS-BH inspiral with far more accuracy than a BH-BH inspiral. Using the Fisher information matrix, we evaluated the accuracy of the parameter estimation obtained using Bayes' theorem to create a GW skymap of the most likely source locations of a GW signal.

4. 3D Localization

Next, we looked at ways of incorporating a source's distance along with its sky location as parameters in Bayes' theorem to determine a 3D skymap of the most probable source locations for low latency source localization. Assuming a uniform prior distribution, we used Bayes' theorem to create a posterior probability distribution for various distance slices ranging from 0 to 400 Mpc in bins of 20. This was done for all events with a false alarm rate less than or equal to 1 per century. We then created a video of the skymaps for each distance slice to analyze how the posterior probability distribution changed over distance. An example of the normalized skymaps for distances slices ranging from 40 to 180 Mpc is shown in Fig. 7.

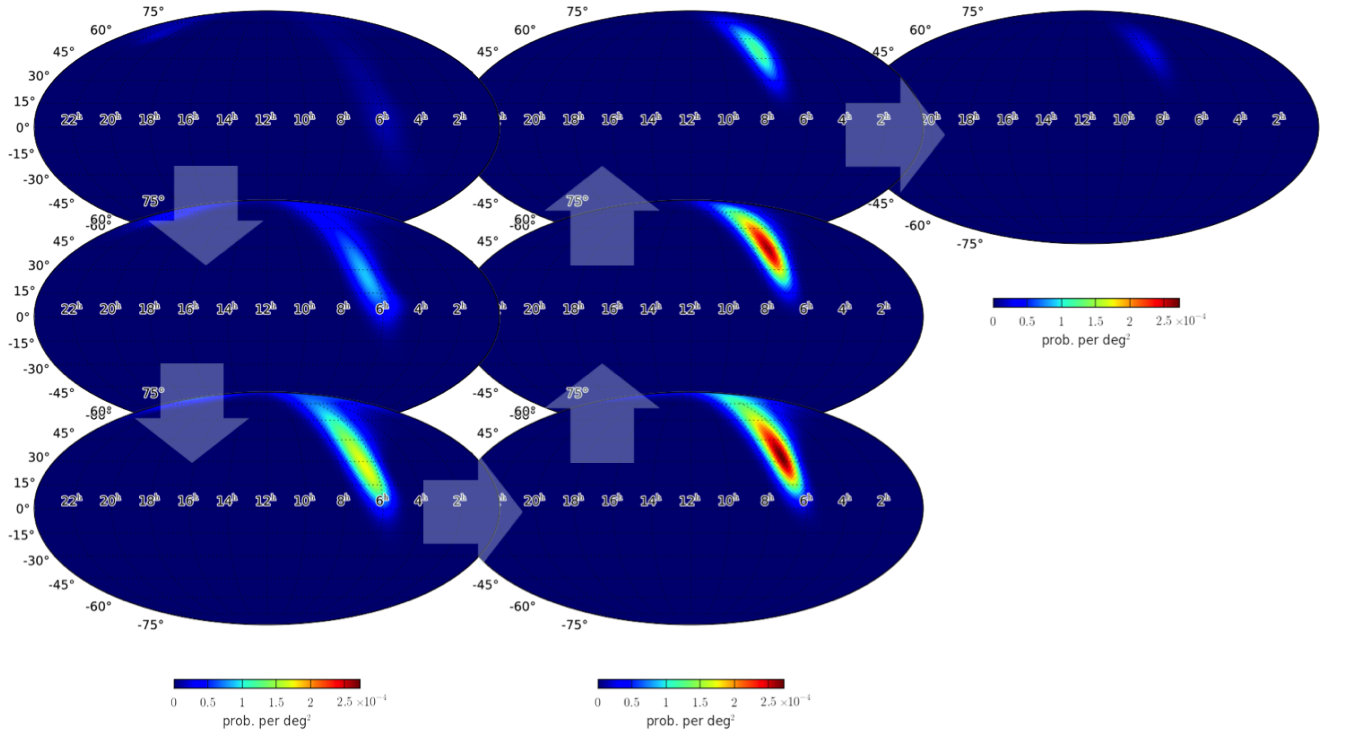


Figure 7: Skymaps of distance slices ranging from 40 to 180 Mpc in bins of 20 for the coincident event 22903.

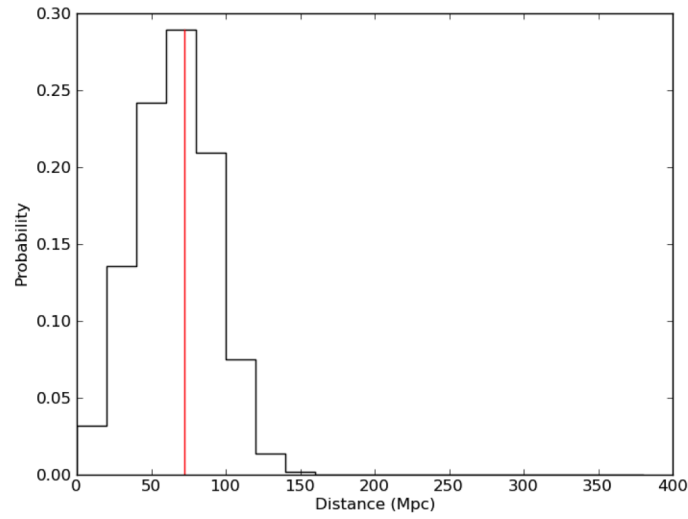


Figure 8: Probability of the source location of coincident event 22903 being located within a given distance slice ranging from 0 to 400 Mpc in bins of 20. The true distance to the source is shown in red.

To evaluate the accuracy of the distance localization for each event, we looked at the total probability of the source being located in each distance slice in comparison to the true distance to the source, an example of which is shown in Fig. 8.

For nearly all observed skymaps, the most probable source locations usually conglomerated into one distinct region, as exemplified by the single highlighted region in each skymap in Fig. 7. To display graphically how the region of most probable sky locations changes with distance, we created a polar plot for each event, where distance is represented along the radial axis and the projection of the most probable ra and dec coordinates of the region are shown along the angular axis. Examples of these polar plots are shown in Figs. 9a and 9b.

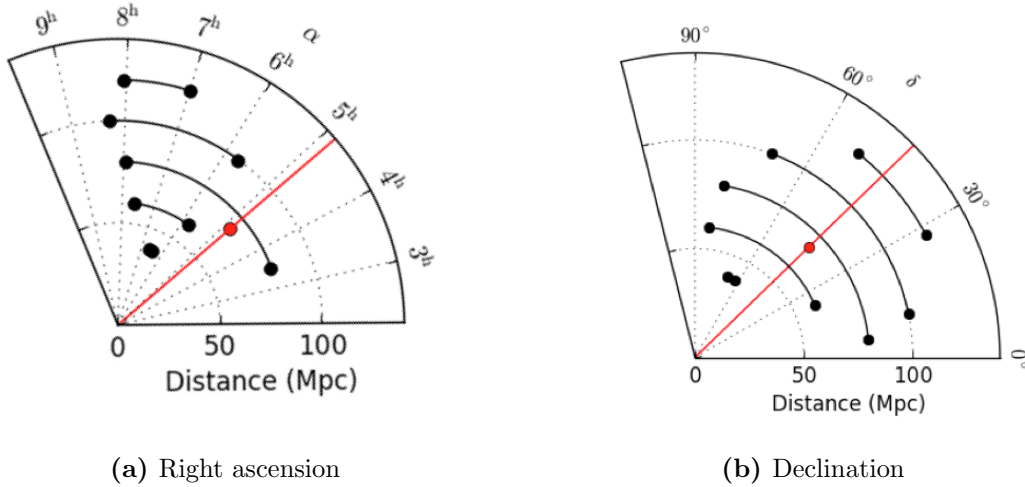


Figure 9: Polar plots of distance versus the most probable ra and dec coordinates. Black dots represent the minimum and maximum ra and dec coordinates of the source’s region of most probable location for the five most likely distance slices ranging from 0 to 400 in bins of 20. The true distance and ra and dec coordinates of the source are denoted by red dots.

As depicted in Fig. 9, this type of plot condenses information about how the width, height, and position of the region of most probable source locations change with distance. These changes in “width” and “height” across distance are indicated by the lengths of the black curves connecting the minimum and maximum most probable ra and dec coordinates in Figs. 9a and 9b respectively. The changes in the position of the region are indicated by the angular shifting of the black curves over distance. As shown in Figs. 9a and 9b, for this particular event, as distance increases the ra coordinates tend to increase and the dec coordinates tend to decrease. However, this change in position was specific to this event. The observed relationship between sky location and distance was not consistent enough across all events to suggest a general trend. On the other hand, there was a consistent relationship observed between the distance and the size of the most probable region. As shown in Figs. 9a and 9b, for nearly all events, the width and height of the region of highest probability increases the closer the distance slice is to the source’s true distance.

In Fig. 10, we analyze the cumulative offset in the source localization accuracy of the posterior probability distribution for all events with false alarm rates less than or equal to 1 per century.

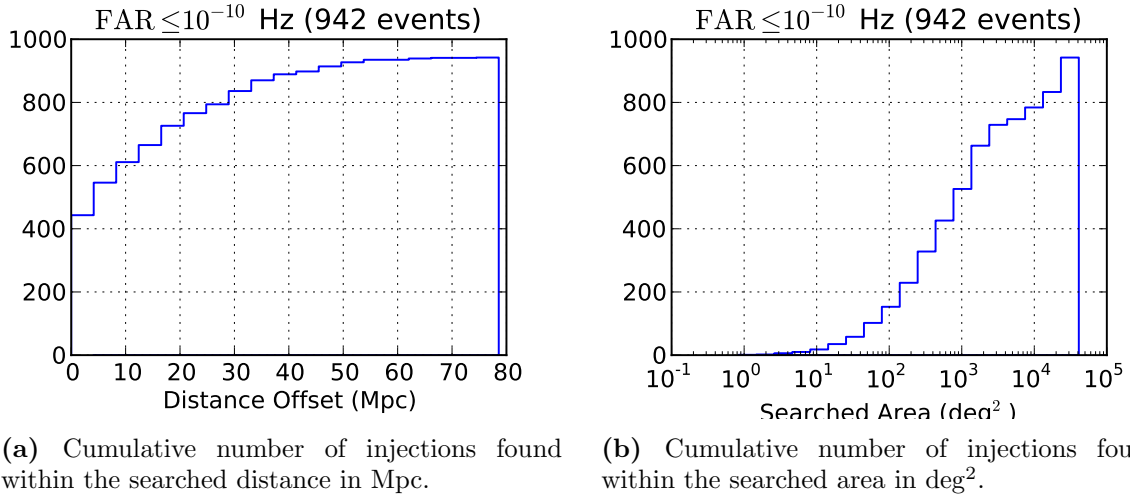
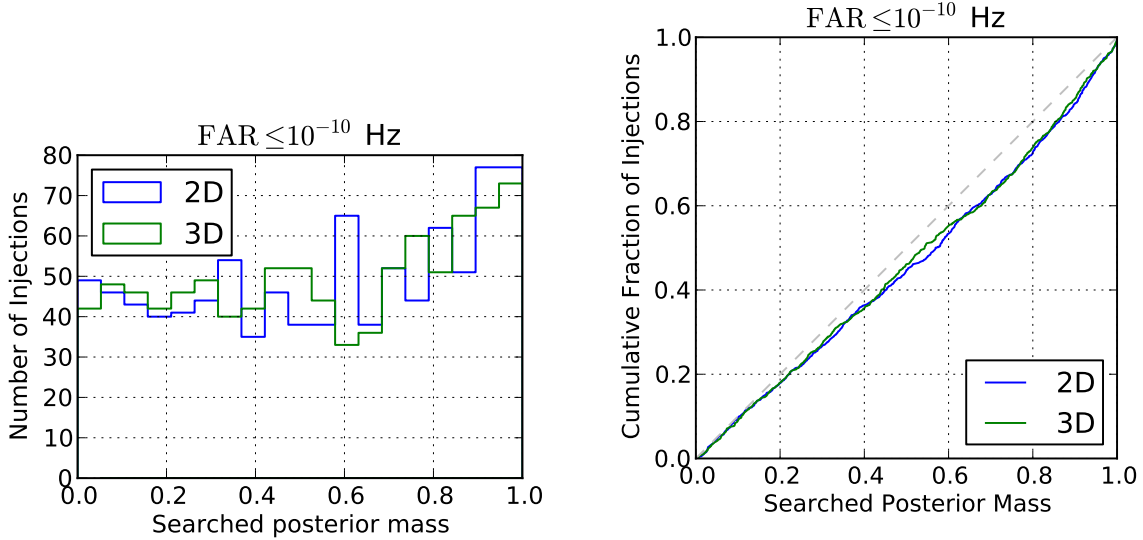


Figure 10: Offset between the mode of posterior and the true location of the source for all events with a false alarm rate less than or equal to 1 per century.

As depicted in Fig. 10a, the 3D posterior probability distribution is able to accurately localize the true distance bin (20 Mpc) to the source for all of the events within approximately 60 Mpc and half of the events within approximately 10 Mpc. In other words, for event candidates with false alarm rates less than or equal to 1 per century, finding the distance to the source of all the events would require searching three distance bins from the mode of the posterior in either direction (approximately 140 Mpc). And finding distance to the source of half the events would require searching a half distance bin from the mode of the posterior in either direction (approximately 40 Mpc). Fig. 10b displays the angle between the sky location of the mode of the posterior and the true ra and dec coordinates. These results indicate that the sky location of all of the events' sources can be found within approximately $10^{4.3} \text{ deg}^2$ and half of the events' sources can be found within 10^3 deg^2 .

To compare the percision of 2D and 3D source localization, we evaluated the number and cumulative fraction of injections found within a given searched posterior mass for both a 2D and 3D posterior probability distribution, as shown in Figs. 11a and 11b respectively. The lines for both the 2D and 3D posterior probability distributions in Fig. 11b curve slightly below the ideal linear relationship, illustrated by the dashed line. However, the cumulative fraction of injections found per searched posterior mass doesn't appear to be adversely affected by requiring distance localization in addition to sky localization.

Future work could focus on creating alternative visulazations of a 3D skymap beyond the polar plots we created. In addition, future studies should look into ways of constructing a prior using information from a galaxy catalog instead of just assuming a uniform prior distribution to further enhance source localization.



(a) Number of injections found within a given searched posterior mass.

(b) Cumulative fraction of injections found within a given searched posterior mass.

Figure 11: Found injections within the searched posterior mass for events with false alarm rates less than or equal to 1 per century. The blue line depicts the number or proportion of injections for which their sky location was found within the searched posterior mass. Whereas, the green line depicts the number or proportion of injections for which their sky location and distance was found within the same searched posterior mass.

5. Acknowledgments

I'd like to thank my mentors Larry Price, Vivien Raymond, and Leo Singer for helping me with this project and I'd also like to thank the NSF and Caltech's SURF Program for giving me the opportunity to work on this project over the summer.

References

- [1] M. Pitkin, S. Reid, S. Rowan, and J. Hough, *Living Rev. Relativity* **14**, 5 (2011).
- [2] The LIGO Scientific Collaboration, *Nature Phys.* **7**, 12 (2011).
- [3] L. Singer, L. Price, and A. Speranza. (2012), arXiv:1204.4510v1 [astro-ph.IM].
- [4] B. F. Schutz, *Class. Quantum Grav.* **16**, A131 (1999).
- [5] B. D. Metzger and E. Berger, *Astrophys. J.* **746**, 48 (2012).
- [6] S. Nissanke *et al.*, *Astrophys. J.* **725**, 1 (2010).
- [7] S. Fairhurst, *New J. Phys.* **11**, 123006 (2009) , arXiv:0908.2356v2 [gr-qc].
- [8] J. Ellis, "A Bayesian analysis pipeline for continuous GW sources in the PTA band," (2013), arXiv:1305.0835v1 [astro-ph.IM] .
- [9] J. Abadie *et al.*, *Astron. Astrophys.* **541**, A155 (2012), arXiv:1112.6005v4 [astro-ph.CO].

- [10] Gravitational-wave Candidate Database, <https://gracedb.ligo.org/events/G71031>.
- [11] L. K. Nuttall and P. J. Sutton, Phys. Rev. **D82**, 102002 (2010), arXiv:1009.1791v3 [gr-qc].
- [12] E. Berger, Astrophys. J. **690**, 231 (2009), arXiv:0805.0306v1 [astro-ph].
- [13] LIGO Document T0900288-v3, https://dcc.ligo.org/public/0002/T0900288/003/ZERO_DET_high_P.txt